Sound & Vibration 2026, 60(4), 4069.
doi: https://doi.org/10.59400/sv4069

Article

Parametric sensitivity analysis of impact-induced vibration in revolving cannon systems using the PCE surrogate model

Junyu Shan[1], Ming Hu[1], Shuai Yue[2,*], Zhonghua Du[1,2], Zihao Wang[2]

[1] School of Equipment Engineering, Shenyang Ligong University, Shenyang 110159, China
[2] School of Mechanical Engineering, Nanjing University of Science and Technology, Nanjing 210094, China
*** Corresponding author:** Shuai Yue, yueshuai@njust.edu.cn

CITATION

Shan J, Hu M, Yue S, et al. Parametric sensitivity analysis of impact-induced vibration in revolving cannon systems using the PCE surrogate model. Sound & Vibration. 2026; 60(4): 4069. https://doi.org/10.59400/sv4069

ARTICLE INFO

Received: 23 February 2026
Revised: 18 April 2026
Accepted: 23 April 2026
Available online: 17 July 2026

Abstract: impact vibration problems brought by impacts between sliding plates and rotating chamber structures when revolver shooting processes go on, a parameterized dynamic model which includes gas-driven mechanisms and curved chamber contact relations has been constructed. The accuracy of the model has been verified by means of chamber pressure measurement experiments and high-speed photography experiments. For overcoming the computation restriction problems of high-precision simulated experiments, a sparse polynomial chaos expansion method has been utilized by us for building a high-accuracy substitute model. In combination with the Sobol global sensitivity analysis method, this research has quantitatively carried out an evaluation of the influence that eight key geometric and physical parameters exert upon maximum collision forces. Our results have shown that the elliptical long axis of recoil chambers is the main parameter that contributes 67.2% to the main effect; what comes next is the elliptical minor axis and linear sections, which have contribution proportions of 17.1% and 10.3% separately. Other parameters have demonstrated influences which can be ignored. The optimization model which is gotten from sensitivity analysis has decreased maximum contact forces by 29.73%, thus its validation errors are under 1% via high-fidelity modeling. This study provides a theoretical basis and efficient analytical tools for structural optimization and impact vibration suppression of turret-mounted guns.

Keywords: revolver system; sparse PCE model; global sensitivity analysis; Sobol analysis; structural optimization

1. Introduction

Rotating-barrel guns are a high fire-rate weapon system that is widely used in the field of air defense. In their working principle, the Y-shaped open groove mainly has the function of guiding and passing on rotating power from automatic firearms. The periodical clash between this groove and the rolling bodies forms a key constituent part to reach accurate angle orientation and continuous shooting [1–3]. The instant impact loads which are produced in the course of these collisions have a direct influence on the precision of barrel rotation, the fatigue life of components, and the dynamic stability of the whole system [4, 5]. Nevertheless, overabundant collisions may bring about stress concentration, structural abrasion, and even early invalidation of key components [6, 7], thus damaging the firing dependability and working life of rotating-barrel systems [8–13]. Therefore, confirming key parameters that have an influence on collision forces of Y-slots and explaining their basic mechanisms has important engineering meanings for improving structure designs of rotating-barrel guns.

Existing research has already proven that the movement rules of automatic weapons fundamentally are a strongly nonlinear multi-body dynamic coupling system, in which reaction results are at the same time affected by gas dynamics, mechanical geometry parameters, and frictional contact behaviors [14–16]. In the research of gas-driven modeling, many scholars have made coupled models that combine gas flow and piston movement on the basis of internal ballistic theory, which have given theoretical bases for forecasting the propulsion force of automatic weapons [17, 18]. After that, multi-body system dynamics methods have gotten broad applications in weapon mechanism motion processes, which analyze system response characteristics through equivalent mass, damping, and stiffness models [19, 20]. Nevertheless, the traditional simplified models still have difficulty accurately depicting the evolution mechanisms of contact forces in rotating chamber mechanisms that have complex spatial curved slot structures [21]. In recent years, the combination of experiment measurement and digital calculation simulation has thus become a key method for the research of automatic weapon movement rules. High-speed photography, cavity pressure measurement, and dynamic signal gathering techniques are utilized by researchers to obtain real-time movement parameters and load data in the working process of weapons [22, 23]. The research shows that, when people use experimental data to verify dynamic models, this behavior can greatly promote the credibility of models [24]. Even so, high-fidelity simulation works often bring about very big calculation costs, and direct depending on numerical models becomes a difficulty for large-scale parameter search in multi-parameter design optimization or uncertainty analysis [25]. For solving the problem of high computation demands, substitute models—which combine analytic expression ability with computation efficiency—are broadly employed for uncertainty spread and sensitivity analysis [26–29]. When compared with conventional response surface methods, PCE can get close to stochastic responses by utilizing orthogonal polynomial basic functions and directly calculating Sobol sensitivity indices, hence enabling analytical evaluation of parameter contributions [30, 31]. This method has obtained successful application in complex engineering systems that contain structural dynamics, fluid-solid coupling, and impact response analysis [32]. But, agent modeling and global sensitivity analysis, which is based on polynomial chaos expansion (PCE), are still comparatively not common in dynamic research of automatic weapons, especially rotating-barrel systems. Current research mostly focuses on drive systems or whole motion performance analysis, whereas the mechanisms that geometric structure parameters affect contact impact forces still have not got enough understanding. It is worthy to note that the geometric parameters of curved slots can influence the distribution of impact loads through the changing of contact paths and kinematic constraint conditions. However, quantitative research works in this domain still have not made enough achievements. Besides this, the systematic global analysis frameworks which are used for finding key influence factors under multi-parameter coupling are still lacking [33, 34]. Current research on automatic weapon dynamics have already acknowledged the intrinsic property of multi-coupled systems. They use modeling methods that integrate internal ballistic theory with multi-body dynamics and meanwhile validate simulation results by means of experiments, and there are also chaotic explosion models used for sensitivity index computation. But, PCE agent models have not been fully used in the analysis and optimization of rotating-barrel mechanism, especially for the structures of complex space curved grooves, where calculation costs still keep high, large-scale optimization is still a difficult problem, and systematic global sensitivity analysis frameworks which are used to find key influence factors under multi-parameter coupling still do not exist.

On the basis of already done research, the present research probes into vibration mechanisms which are caused by sliding plate collision with rotating chamber structures when rotating chamber guns carry out work, through the method of dynamic modeling and parameter sensitivity analysis. Firstly, one parameterized dynamic model which includes gas-pushed mechanisms and curved groove contact interactions is built, with model verification being carried out through chamber pressure measuring experiments and high-speed photograph experiments. Second, the sparse polynomial chaos expansion method is utilized to build high-accuracy substitute models, thus effectively decreasing calculation expenses that are connected with high-fidelity simulations. Finally, through utilizing the Sobol global sensitivity analysis method, we carry out quantitative assessment of the influence modes of key geometric and physical parameters on the maximum collision force, and in the meanwhile, we make clear the coupling mechanisms between important parameters.

2. Parametric dynamics modeling and experimental validation

2.1. Parametric dynamics model

2.1.1. Model assumptions and establishment

On the basis of guaranteeing an objective depiction of physical occurrences, the model uses the following basic suppositions: the sliding plate, the rotating chamber, and the rollers are processed as rigid bodies; the gas that gunpowder produces is regarded as a perfect gas, which has one-dimensional stable adiabatic flowing inside the gas channel; the friction that exists on contact surfaces follows Coulomb's law; the secondary losses are put into neglect; the slip board carries out translation movement along the x-direction, meanwhile, the rotation cabin carries out rotation around a fixed axis.

The vibration characteristics of revolver mechanisms primarily result from collision forces between the slide plate and rotating chamber structure. **Figure 1** illustrates the force distribution during the recoil process, while **Figure 2** depicts the force distribution during the return stroke. Key parameters include: a_1 and b_1 representing the major/minor axes of the recoil elliptical slot; a_2 and b_2 for the return elliptical slot; S_1 and S_2 indicating the linear segments of recoil and return motions. The recoil direction is defined along the positive x-axis, with variables including: Fp (piston force), F_f (friction force), v (slide plate velocity), x (displacement distance), k (spring stiffness), F_k (spring force), β (parameter introduced for computational convenience), F_t (tangential force exerted by the slide plate on the rotating chamber), θ (angle between the normal vector at the roller-contact point and the x-axis), μ (friction coefficient), ω (rotating chamber angular velocity), R_t (rotating chamber radius), R_b (center-to-slide plate curve slot radius), and α (rotating chamber angle).

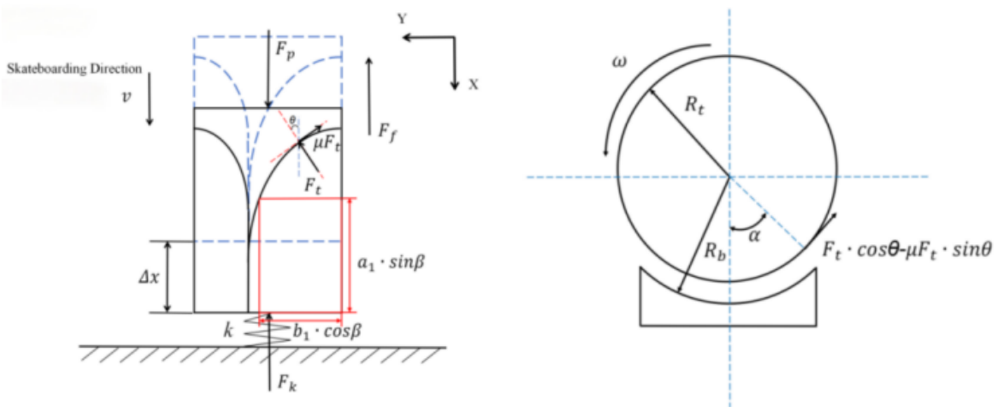

Figure 1. Force diagram during recoil pro.

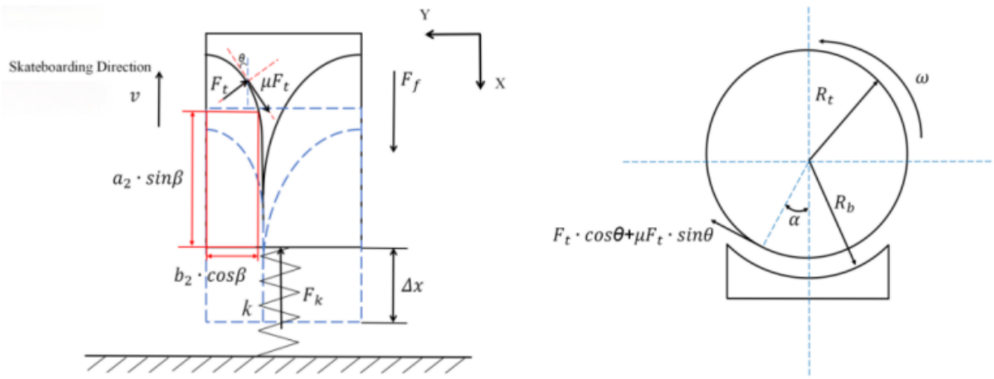

Figure 2. Force diagram during the re-entry process.

The kinetic equation is:

$$m_{eq}\ddot{x} + c_{eq}\dot{x} + k_{eq}x = F_{gen}. \tag{1}$$

In the formula F_{gen} represents the generalized force. c_{eq}, m_{eq}, k_{eq} are equivalent mass, damping, and stiffness, respectively, with the corresponding expressions as follows:

$$\begin{cases} m_{\mathrm{eq}} = m + \dfrac{I}{R_b^2} \\ c_{\mathrm{eq}} = \dfrac{\mu I \omega}{R_b^2} \\ k_{\mathrm{eq}} = k + \dfrac{\partial F_t}{\partial x} \\ F_{\mathrm{gen}} = F_p - \mu F_t \sin\theta \end{cases} \tag{2}$$

2.1.2. Geometric relationships and supplementary equations

The geometric relationship of the groove curve is expressed by the ellipse formula:

$$\begin{cases} \dfrac{(x - S_1)^2}{a_1^2} + \dfrac{y^2}{b_1^2} = 1 \\ \dfrac{(x - S_2)^2}{a_2^2} + \dfrac{y^2}{b_2^2} = 1 \end{cases} \tag{3}$$

Other auxiliary supplementary equations are:

$$\begin{cases} \tan\theta = \left|\frac{dx}{dy}\right| = \frac{b_1^2(x-S_1)}{a_1^2 y(x)} \\ \tan\theta = \left|\frac{dx}{dy}\right| = \frac{b_2^2(x-S_2)}{a_2^2 y(x)} \\ F_t = F_n \cdot \sin\theta \\ F_k = k \cdot x \\ F_f = \mu \cdot F_n \cdot \cos\theta \end{cases} \tag{4}$$

The rotating chamber has a moment $\mathrm{kg} \cdot \mathrm{m}^2$of inertia of 0.092 kg·m^2, with the radius from its center to the sliding plate being 0.095 m. The sliding plate weighs 3.1 kg and has a rotating chamber radius of 0.096 m. The spring stiffness is 650.23 N/m. The recoil elliptical slot measures 0.1 m in length and 0.0655 m in width, while the reentry elliptical slot measures 0.064 m in length and 0.04 m in width. The linear segments for recoil and reentry are 0.04 m and 0.076 m, respectively. The mapping relationship between input parameters of the dynamic model and PCE agent model parameters is detailed in **Table 1**.

Table 1. Mapping relationship between input parameters of the kinetic model and parameters of the PCE agent model.

Variables in the model	Physical significance	Corresponding PCE parameter symbol
a_1	Long axis of the retrospinal groove	X_3
b_1	Short axis of the retroacromial groove	X_4
S_1	Straight-line segment of backward motion	X_5
a_2	long axis of reentry groove	X_6
b_2	short axis of reentry groove	X_7
S_2	Re-enter straight segment	X_8
k	spring rate	X_1
μ	friction factor	X_2

The pressure calculation formula acting on the gas-guiding piston is:

$$\dot{m}_g = C_d \cdot A_d \cdot \sqrt{\frac{2\gamma p_b}{\gamma R T_b} \cdot \left(\frac{2}{\gamma+1}\right)^{\frac{\gamma+1}{\gamma-1}}}, \tag{5}$$

$$p_g = \frac{m_g R T_g}{V_0 + A_p x_p}. \tag{6}$$

The physical symbols involved in the formula are listed in **Table 2**. Key parameters include: gas $0.00003\ \mathrm{m}^2, 280\ \mathrm{J/(kg \cdot K)}, 1,600\ \mathrm{K}, 0.00071\ \mathrm{m}^2, 0\ \mathrm{m}^3, 10,132\ \mathrm{Pa}$ flow coefficient of 0.8 for the gas guide orifice, cross-sectional area of the gas guide orifice, gas constant of gunpowder gas, chamber gas temperature, adiabatic index of gunpowder gas (1.25), piston area, and initial chamber volume assumed to be constant (with machining errors neglected). Environmental atmospheric pressure is specified, while the piston surface pressure is calculated using experimentally measured chamber pressure as input data.

Table 2. Meaning of physical symbols.

Symbol	Physical significance	Unit
m_g	Gas mass in the air chamber	kg
p_g	Cavity pressure	Pa
x_p	Piston displacement/slab displacement	m
$\dot{m}_g$	Mass flow rate entering the gas chamber through the gas inlet port	kg/s
C_d	Flow coefficient of gas venting port	dimensionless
A_d	Cross-sectional area of gas vent	m^2
p_b	breech pressure	MPa
R	Gas Constant of Gunpowder Gas	J/(kg·K)
T_b	In-cylinder gas temperature	K
γ	Adiabatic Index of Gunpowder Gas	dimensionless
A_p	Piston cross-sectional area	m^2
V_0	Initial volume of the air chamber	m^3
p_a	Ambient atmospheric pressure	Pa

The contact force model between the roller and the curved groove adopts the modified Hertz model:

$$F_n = K_h \delta^{\frac{3}{2}} + D_h \dot{\delta} \tag{7}$$

In the formula, F_n represents the contact force, δ represents the penetration depth, which is set to 0.1, K_h represents the contact stiffness, which is set to 100,000, and D_h represents the damping coefficient, which is set to 50.

2.2. Experimental validation

2.2.1. Chamber pressure testing experiment

The chamber pressure testing apparatus comprises a ballistic cannon, a Kistler 6215 pressure measurement sensor (accuracy: ±0.5% FS, range: 0–500 MPa), a dynamic signal testing and analysis system, and a data storage device, as illustrated in **Figure 3**. Seven tests were conducted: the first two were for equipment verification, while the average values of data collected at each time point from the subsequent five tests are presented in **Figure 4**. The chamber pressure peak has maintained for 4.26 ms. There is a fast pressure rise at time 0. After that, there is a pressure flat stage, which is about 142 MPa during 0.09–0.18 ms. In the five effective experiments, the cavity pressure maximum showed a standard deviation of 3.2 MPa, having a variation coefficient (CV) of 1.8%, hence the muzzle pressure standard deviation was 1.5 MPa, hence all of them show that the performance is acceptable.

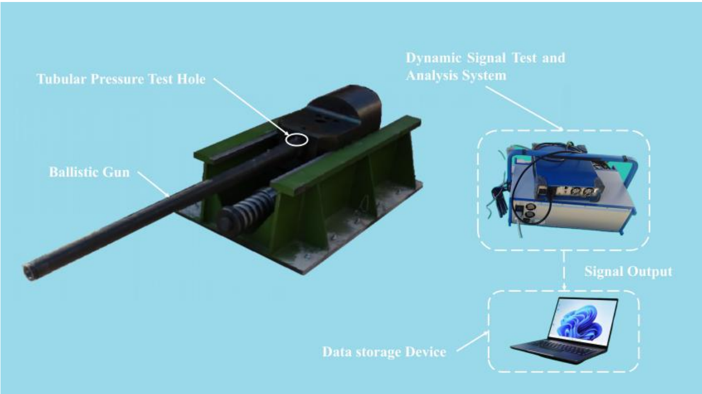

Figure 3. Test diagram of the pressure chamber test device.

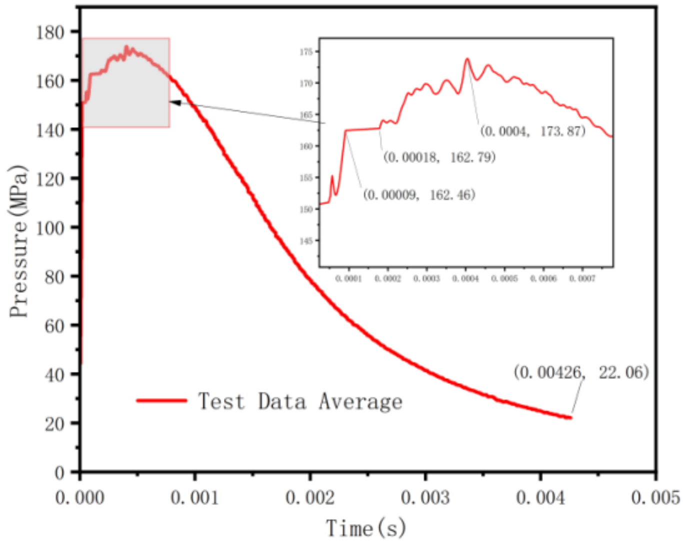

Figure 4. P-t curve of a ballistic gun.

2.2.2. Kinetic model validation test

The dynamic examination of the rotating cannon turret is shown in **Figure 5**. The experiment's setting contains high-speed photographing apparatuses, a revolving turret gun platform, and the real revolving turret gun itself. High-speed photography catches the working procedure of the rotating turret gun, with proportion conversion and least square fitting methods that are applied to obtain the angle rotation-time curve. The marked points which correspond to 72°rotations of the turret were obtained in equally spaced intervals, thus the video frame rates and the real-time stamps were recorded to build the relationship between angle and time. Relative positions of the sliding plate and the rotating turret have been measured before and after every test cycle, thus to guarantee the alignment of components and the accuracy of data.

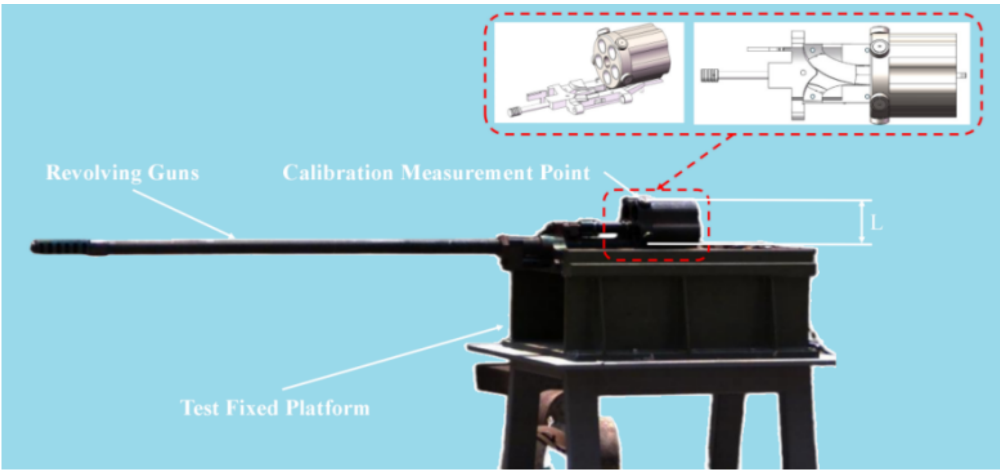

Figure 5. Site installation diagram.

Figure 6 shows the partial image outcome that comes from the high-speed photography part (frames 1–221), with six images being output at 47-frame gaps. The first picture catches the time point when the shooting projectile just starts, after that, the rotating cavity part starts its movement at frame 65, and the first round finishes at frame 236 when the rotating cavity part finishes a rotation of 72°.

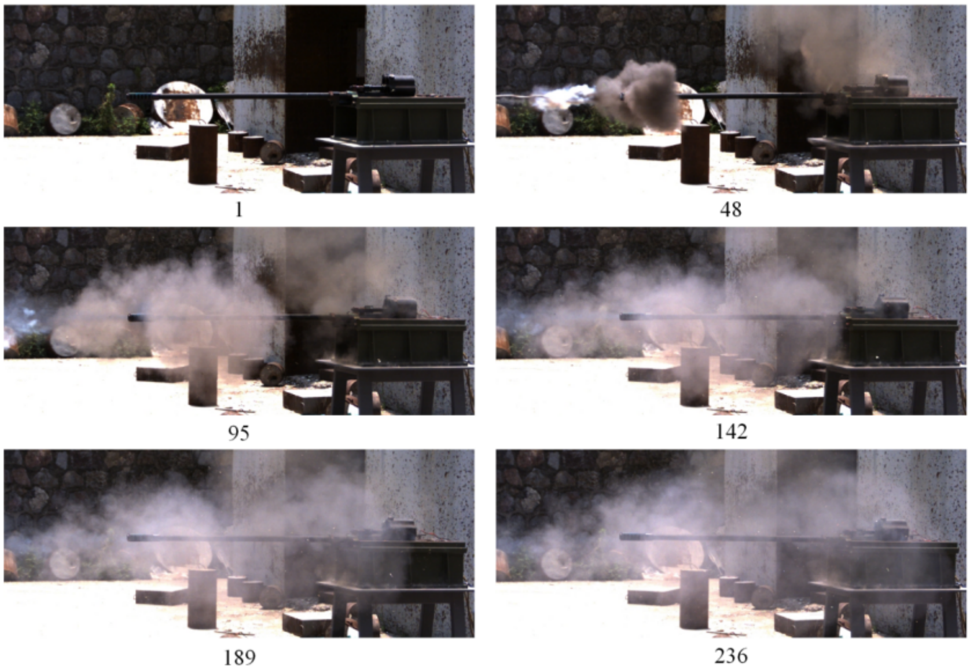

Figure 6. Partial image output from the high-speed photography section.

The bolt carrier starts its rotating motion at 0.0154 s, arrives at 72° at 0.0232 s, stays motionless for 0.0178 s before it enters the next firing cycle with the rotation angle being reset to zero, hence completing the first firing cycle. The bolt carrying component commences its rotation once more at 0.056 s, attains a 72° rotational angle at 0.064 s, and therefore finishes the second firing cycle at 0.082 s. The rotational movement time length for two ignition work cycles is 0.0078 s and 0.008 s, with both two cycles arriving at 72° rotation angle values.

2.2.3. Validation of the dynamics model

On the basis of Pearson correlation coefficient, RMSE, and temporal similarity similarity test methods, the weighted average method is utilized by us to compute the total similarity, wherein weight design follows the principle of "core feature first". The formula which is used for calculating the total similarity is just as below:

$$S_{overall} = \omega_{peak} \cdot S_{peak} + \omega_{trend} \cdot S_{trend} + \omega_{linear} \cdot S_{linear} + \omega_{temp} \cdot S_{temp}. \quad (8)$$

In the formula, the peak similarity weight is set to 0.25, the temporal similarity weight to 0.2, the linear similarity weight to 0.3, and the trend similarity weight to 0.25. The similarity levels are categorized as: when $S_{overall} \geq 90\%$ is extremely similar, when $80\% \leq S_{overall} < 90\%$ is highly similar, when $70\% \leq S_{overall} < 80\%$ is moderately similar, when $60\% \leq S_{overall} < 70\%$ is slightly similar, and when $S_{overall} < 60\%$ is almost dissimilar [35,36].

Because of the restrictions on sensor installation that stop the direct measurement of roller-groove contact force, an indirect checking method was utilized by us. The rotational chamber angle acceleration which was obtained by high-speed photography was utilized to get the tangential force that acts on the rotating chamber through dynamic equations. The contact force Fn was afterward computed through algorithms of geometric relation transformation. Simulation forecast results showed the biggest contact force of 1.38×10^5 N, hence the calculated value was 1.32×10^5 N, hence the relative deviation is 4.5%, which is within the scope that people can accept.

Figure 7 does the comparison between simulation data and experimental data on the rotational angle change of the rotating cylinder with the passing of time. Two curves all display basic consistency in frequency and amplitude features. However, although the simulation curve displays smooth changes in the starting and ending stages of the rotating part's movement, the experiment curve has clear turning points. In addition, the simulation curve displays a steeper gradient in the rising stage when compared with the experimental data. This difference may come from excessively idealized assumptions about driving force and accumulated errors that are brought by the accumulation of system clearance.

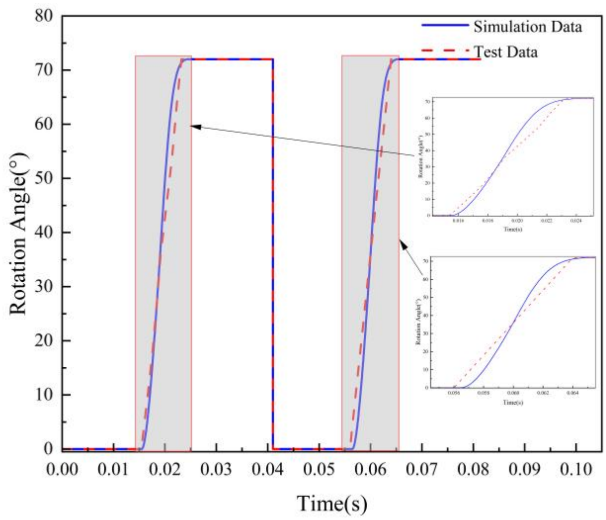

Figure 7. Comparison between simulation data and experimental data.

Figure 8 shows the difference curve that lies between the simulation curve and the test curve along with the change of time. In the time interval of 0.015 to 0.023 s, small undulations have been observed by us between the two curves, and the minimum value and maximum value are respectively recorded at 0.017 s (−4.29) and 0.021 s (+10.44). Similar small undulations took place in the 0.056–0.064 s interval, in which the smallest and largest values showed themselves at 0.058 s (−8.55) and 0.062 s (+7.94), separately.

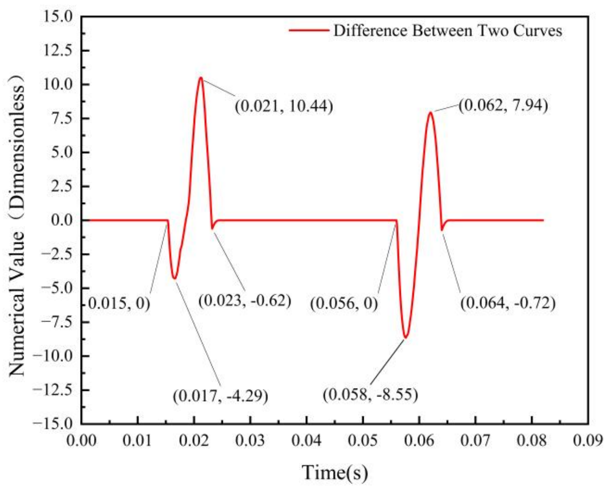

Figure 8. Difference curve between simulation and test curves over time.

The Pearson correlation coefficient, which is 0.9893 (close to 1), shows a strong positive correlation, while the RMSE value, which is 0.0062, proves that the mathematical model has extremely small prediction errors, so it confirms high linear fitting accuracy. The similarity coefficient of time series attains 0.9984. Equation (6) makes known that the whole similarity coefficient is 0.9285, and all measurement indicators are within the reference ranges; only RMSE has a small exceeding of the threshold. When we consider whether the theoretical model conforms to high-precision demands, the dynamic model that we have built shows strong accuracy, hence it gives a firm theoretical basis for the research that comes after.

3. Proxy modeling and sensitivity analysis framework based on PCE

3.1. Parameter space and sampling design

On the one hand, when we think about engineering practice, the lack of existing prior information requires that we use a uniform distribution in accordance with the maximum entropy principle to make the bias become smaller. On the opposite side, the even distribution makes possible an estimation without bias for the average contribution that parameters give within the design space. Finally, the Legendre polynomial basis functions are utilized by us to carry out fitting. To make the long story short, we have the assumption that all parameters obey a uniform distribution in the ranges which are defined for them.

Based on the aforementioned assumptions, an analytical framework integrating polynomial chaos expansion and global sensitivity analysis was constructed. The parameter space defined by eight key parameters X = [X1, X2, ..., X8] is presented in **Table 3**, with each parameter following a uniform distribution within its specified range.

$$X_i \sim U(a_i, b_i), i = 1, 2, ..., 8. \tag{9}$$

Table 3. Detailed definition of parameter space.

Parameter symbol	Unit	Excursion	Base line value	Parameter type	Number of sampling points
a_1	mm	[90,110]	100	Continuation	150
b_1	mm	[59,72]	65.5	Continuation	150
S_1	mm	[36,44]	40	Continuation	150
a_2	mm	[58,70]	64	Continuation	150
b_2	mm	[47,58]	52.5	Continuation	150
S_2	mm	[68,84]	76	Continuation	150
k	N/m	[585,715]	650.23	Continuation	150
μ	Dimensionless	[0.495, 0.605]	0.55	Continuation	150

Four sample groups were established with sample sizes of 500, 1,000, 1,500, and 2,000, respectively, and the coefficient of determination for each group was calculated. The coefficient values for the four groups were 0.98491, 0.98471, 0.98482, and 0.98474, respectively. The variation range of these coefficients remained below 0.0002 across all groups. Notably, the coefficient values began to decrease and stabilized from the N = 1,500 sample size onward. Therefore, a hierarchical adaptive method was employed to generate 1,500 sample sets to construct the dataset.

$$B = \{(X^{(j)}, Y^{(j)})\}_{j=1}^{N}, \tag{10}$$

where Y denotes the maximum collision force.

3.2. Construction of sparse PCE model

The agent model is constructed based on B using polynomial chaos expansion. PCE approximates the output Y as a weighted sum of a multivariate orthogonal polynomial basis:

$$Y \approx M^{\mathrm{PCE}}(X) = \sum\nolimits_{\alpha \in A} c_\alpha \Psi_\alpha(X). \tag{11}$$

Here, is $\alpha = (\alpha_1, ..., \alpha_8)$ the multiple exponent, c_α is the expansion coefficient, and A denotes the selected set of exponents, with:

$$\Psi_\alpha(X) = \prod\nolimits_{i=1}^{8} \psi(i)_{\alpha_i}(X_i). \tag{12}$$

In the formula, $\psi_{\alpha_i}^{(i)} X_i$ denotes the univariate orthogonal polynomial basis corresponding to X_i. Since X_i follows a uniform distribution follows, Legendre polynomials are selected, which satisfy the orthogonality condition:

$$\int_{a_i}^{b_i} \psi_m^{(i)}(x)\psi_n^{(i)}(x)w_i(x)dx = \left\langle \psi_m^{(i)}, \psi_n^{(i)} \right\rangle = \delta_{mn}\gamma_m^{(i)}, w_i(x) = \frac{1}{b_i - a_i} \tag{13}$$

The coefficients c_α are determined through regression. Equation (13) is discretized at sample points to form a linear system:

$$Y = \Psi c + \varepsilon, \Psi_{j,k} = \Psi_{\alpha_k}(X(j)) \tag{14}$$

The coefficient model was established using a least squares regression model with a double truncation scheme. The polynomial had a maximum total degree of p = 3, candidate base terms of p = 165, and a truncation threshold of 1 × 10^{-4}. The actual retained non-zero terms numbered 47, yielding a sparsity of approximately 28.5%. Important terms were adaptively selected from the candidate set to form matrix *A*, resulting in the sparse coefficient vector $\widehat{c}$. The total variance output can be approximated as:

$$D = \mathrm{Var}[Y] \approx \sum\nolimits_{\alpha \in A, \alpha \neq 0} c_\alpha^2 \langle \Psi\alpha, \Psi\alpha \rangle. \tag{15}$$

3.3. Sobol index and uncertainty quantification

The first X_i-order Sobol index for the main effect of parameters is:

$$S_i = \frac{1}{D} \sum\nolimits_{\alpha \in A_i} c_\alpha^2 \langle \Psi\alpha, \Psi\alpha \rangle, A_i = \{\alpha \in A : \alpha_i > 0, \alpha_{j \neq i} = 0\}. \tag{16}$$

The total effect Sobol index is:

$$S_{T_i} = \frac{1}{D} \sum\nolimits_{\alpha \in A_{T_i}} c_\alpha^2 \langle \Psi\alpha, \Psi\alpha \rangle, A_{T_i} = \{\alpha \in A : \alpha_i > 0\}. \tag{17}$$

To compare the independent effects and interaction effects of distinguishable parameters between S_i and S_{T_i}, we employed the leave-one-out method and cross-validation. The Bootstrap method was used to estimate 95% confidence intervals, with a 500-replication bootstrap sample size of 1,500. For each bootstrap sample, the models constructed were analyzed to determine main effects and total effects, with confidence intervals defined as the lower bound at 2.5% and upper bound at 97.5%. The dataset was randomly divided into training and test sets. Evaluation was conducted using the coefficient of determination and root mean square error.

$$R^2 = 1 - \frac{\sum_{j=1}^{N_{test}} \left(Y^{(j)} - \widehat{Y}^{(j)}\right)^2}{\sum_{j=1}^{N_{test}} \left(Y^{(j)} - \bar{Y}\right)^2}, \quad \bar{Y} = \frac{1}{N_{test}} \sum\nolimits_{j=1}^{N_{test}} Y^{(j)}, \tag{18}$$

$$\text{RMSE} = \sqrt{\frac{1}{N_{test}} \sum\nolimits_{j=1}^{N_{test}} \left(Y^{(j)} - \widehat{Y}^{(j)}\right)^2}. \tag{19}$$

Meanwhile, cross-validation with a 10-fold split was employed to evaluate model stability, ensuring the reliability of the results.

4. Simulation results and analysis

4.1. Accuracy of the PCE agent model (corresponding speed)

Figure 9 presents the validation set's residual distribution and prediction plot, with the left panel showing residual scatter points, and the right displaying predicted values. The residual plot reveals that residual values cluster around zero with a uniform distribution, showing no monotonic increasing or decreasing trends. The residual range spans from −5,806.75 N to 8,421.92 N. The predicted values scatter graph demonstrates an R^2 value of 0.978 on the test set, RMSE of 2,197.75 N, and MAPE of 1.27%. On the validation set, predicted and actual values converge near the 1:1 line, indicating good predictive performance.

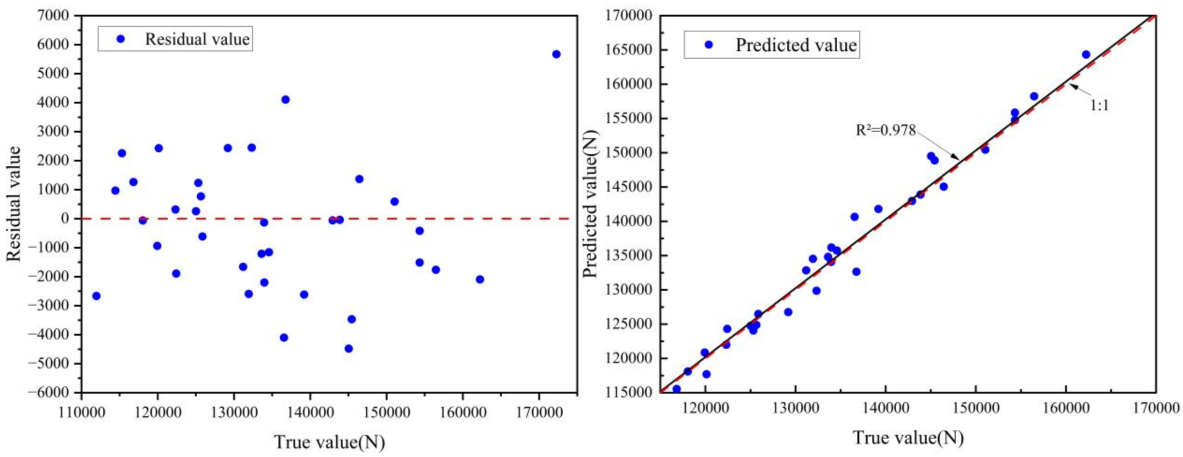

Figure 9. Validation set prediction and residuals.

As shown in **Figure 10**, the coefficient of determination for 10-fold cross-validation ranges from 0.941 to 0.988, with a mean value of 0.972, a median value of 0.973, and a standard deviation of 0.011. The root mean square error values range from 1,823.03 N to 3,336.75 N, with mean values, medians, and standard deviations of 2,732.15 N, 2,751.23 N, and 400.32 N, respectively.

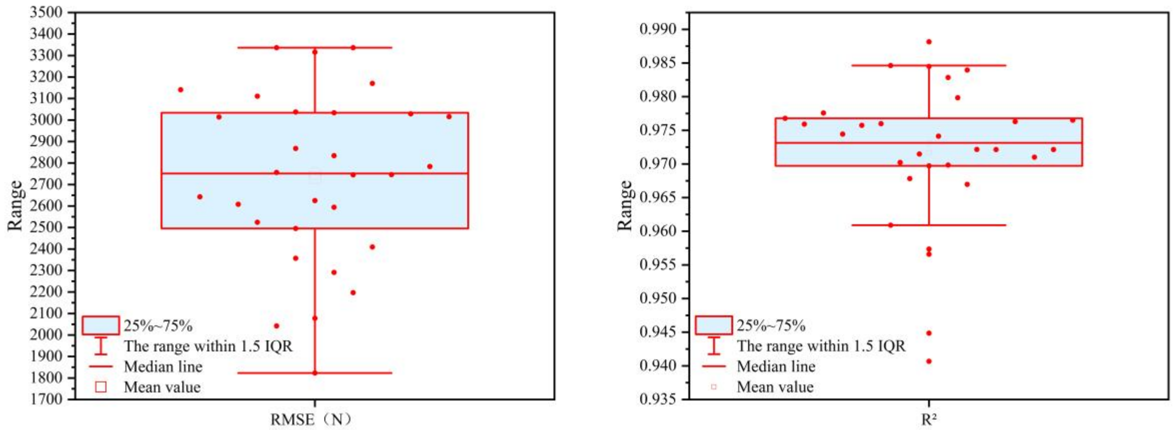

Figure 10. Cross-validation result diagram.

The comparison of three models (PCE, GP, and RBF) across four metrics—R^2, RMSE, prediction time, and fitting time—is presented in **Table 4**. The results demonstrate that the PCE model architecture enhances fitting and prediction efficiency while maintaining computational accuracy.

Table 4. Comparison of model efficiency.

Name	PCE model	GP model	RBF model
R^2	0.9784	0.9784	0.8721
RMSE	2,197.75 N	2,195.09 N	5,348.48 N
Prediction time	0.00004 s	0.00202 s	0.00069 s
Fit time	0.00104 s	0.09682 s	0.00310 s

4.2. Results of global sensitivity analysis

Global sensitivity analysis results are presented in **Table 5**, which quantitatively displays the main effects and total effects of eight parameters. Among them, the μμ main effect and total effect of a_1 are significantly the largest, exceeding 0.6, followed by b_1 and S_1 with values ranging from 0.1 to 0.2 (approximately 0.045), while a_2, b_2, S_2, and k exhibit relatively small values approaching zero. Sobol analysis was conducted with three parameter ranges for a_1: [85,115], [90,110], and [95,105], yielding sensitivity indices of 0.703, 0.672, and 0.641, respectively. Results indicate that although contribution rates decrease with narrower a_1 ranges, these parameters remain dominant. Based on existing dimensional specifications and tolerance requirements, the study selects a range of 90–110 mm. The calculation results for second-order Sobol interaction effect indices are shown in **Table 6**.

Table 5. Global sensitivity index and confidence interval.

Parameter	Main effect	95% CI	Gross effect	95% CI
a_1	0.672	[0.643, 0.700]	0.681	[0.652, 0.712]
b_1	0.171	[0.148, 0.186]	0.177	[0.156, 0.193]
S_1	0.103	[0.084, 0.118]	0.108	[0.090, 0.125]
a_2	0.00014	[0.00002, 0.0017]	0.00093	[0.0009, 0.0063]
b_2	0.00042	[0.00002, 0.0025]	0.00075	[0.0007, 0.006]
S_2	0.00016	[0.00002, 0.0017]	0.002	[0.0009, 0.0077]
k	1.910–5	[0.00002, 0.0011]	0.00203	[0.0010, 0.0084]
μ	0.0401	[0.029, 0.052]	0.0429	[0.0342, 0.0553]

Table 6. Calculation results of second-order Sobol interaction effect index.

Row	a_1	b_1	S_1	a_2	b_2	S_2	Ks	ub
a_1	0.00000	0.00372	0.00321	0.00010	0.00003	0.00008	0.00056	0.00078
b_1	0.00372	0.00000	0.00126	0.00000	0.00003	0.00018	0.00005	0.00083
S_1	0.00321	0.00126	0.00000	0.00004	0.00002	0.00001	0.00010	0.00015
a_2	0.00010	0.00000	0.00004	0.00000	0.00017	0.00010	0.00003	0.00036
b_2	0.00003	0.00003	0.00002	0.00017	0.00000	0.00000	0.00007	0.00002
S_2	0.00008	0.00018	0.00001	0.00010	0.00000	0.00000	0.00097	0.00050
Ks	0.00056	0.00005	0.00010	0.00003	0.00007	0.00097	0.00000	0.00023
ub	0.00078	0.00083	0.00015	0.00036	0.00002	0.00050	0.00023	0.00000

4.3. Analysis of coupling effects of key parameters

Since a_1, b_1, S_1 the sensitivity indices of these three parameters are significantly higher than those of the other five influencing factors, we focus on analyzing their interrelationships. The right axis represents the percentage change in F_{max} (i.e., the impact of a 1 mm displacement on maximum contact force), while the left axis shows the predicted maximum contact force by PCE. Considering manufacturing constraints and workpiece dimensions, a 1 mm adjustment is unaffected by tolerances or process variations, as shown in **Figures 11–13**.

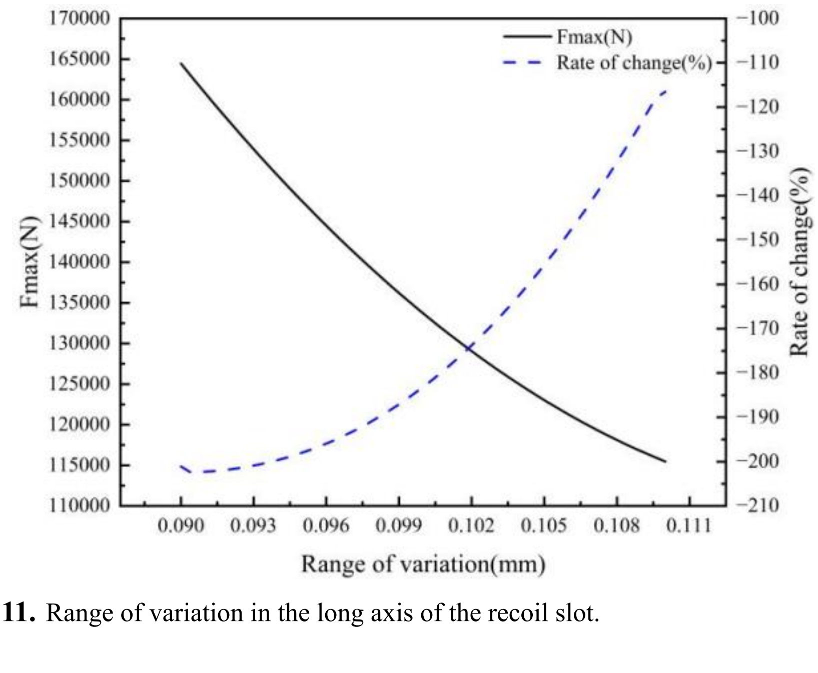

Figure 11. Range of variation in the long axis of the recoil slot.

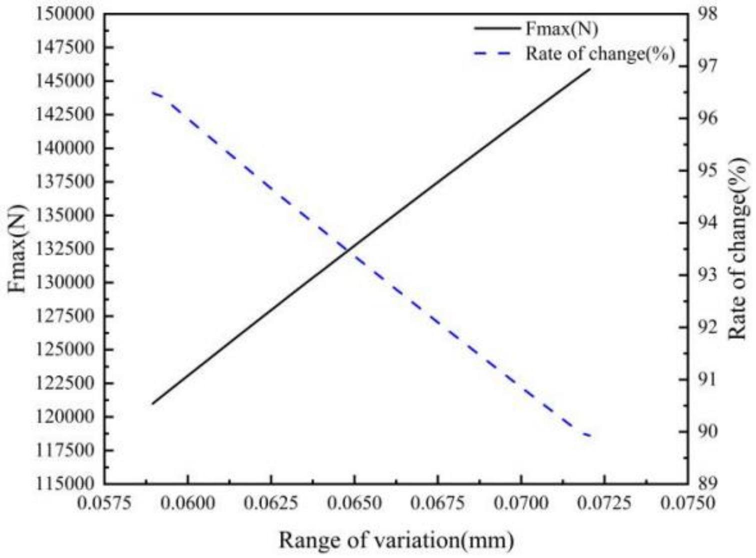

Figure 12. Range of short axis variation in the recoil curve slot ellipse.

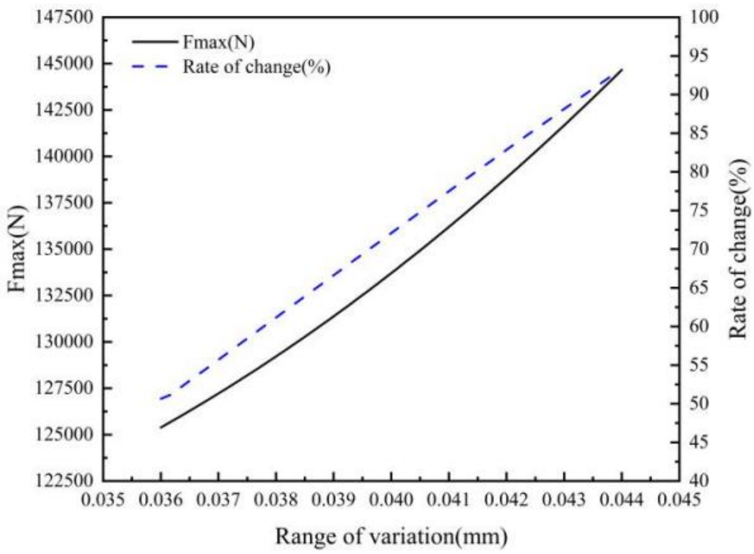

Figure 13. Range of variation in the straight segment of the recoil curve slot.

As shown in the range of rear slot long axis variation in **Figure 11**, the maximum contact force exhibits a significant monotonic decline with increasing values within the 90–110 mm range, decreasing from 1.65×10^5 N to 1.15×10^5 N, representing a 30% reduction. The percentage change in F_{max} rises from −200% to approximately −115%, with a marginal decrease observed at higher end values, indicating a slightly weaker marginal load reduction effect.

As shown in the range of short-axis variation of the recoil curve slot ellipse in **Figure 12**, the maximum contact force exhibits a significant monotonic downward trend within the range of 60–70 mm as the numerical value increases. The maximum contact force decreases by 30% from 1.2×10^5 N to 1.45×10^5 N. The percentage change of F_{max} decreases from 96.5% to approximately 89.8%, indicating a relatively stable overall change.

As shown in the linear segment variation range of the recoil curve slot in **Figure 13**, the maximum contact force exhibits a significant monotonic decreasing trend within the range of 35–45 mm as the numerical value increases. The maximum contact force decreases by 30%, rising from 1.25×10^5 N to 1.45×10^5 N. The percentage change of F_{max} remains positive throughout the entire range and increases with the elastic value as S_1 increases.

As shown in **Figure 14**, the maximum contact force reaches its peak value of 195,588.3 N when S_1 = 44 mm, a_1 = 90 mm, and b_1 = 72 mm. The minimum contact force occurs at 102,436.4 N when S_1 = 36 mm, a_1 = 110 mm, and b_1 = 59 mm. Key parameters include: average contact force (136,347.0 N), standard deviation (17,698.8 N), response amplitude (93,151.9 N), and coefficient of variation (CV = 13%). The maximum contact force increases with increasing values of S_1 and a_1 while decreasing with b_1.

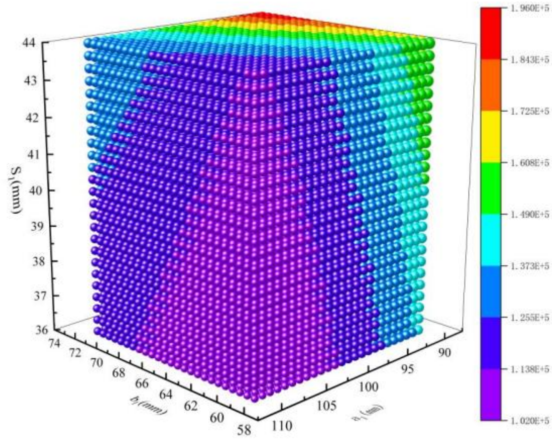

Figure 14. Joint effect scatter plot.

The overall level of contact force gradually increases with increasing slice numbers, and the differences in extreme values within each slice are relatively small. This indicates that under fixed parameter conditions, the sensitivity of contact force to residual variables is relatively limited. The combined variation of a_1 and b_1 dominates the contact force, while S_1 introduces systematic bias within a certain range, as shown in **Figure 15**.

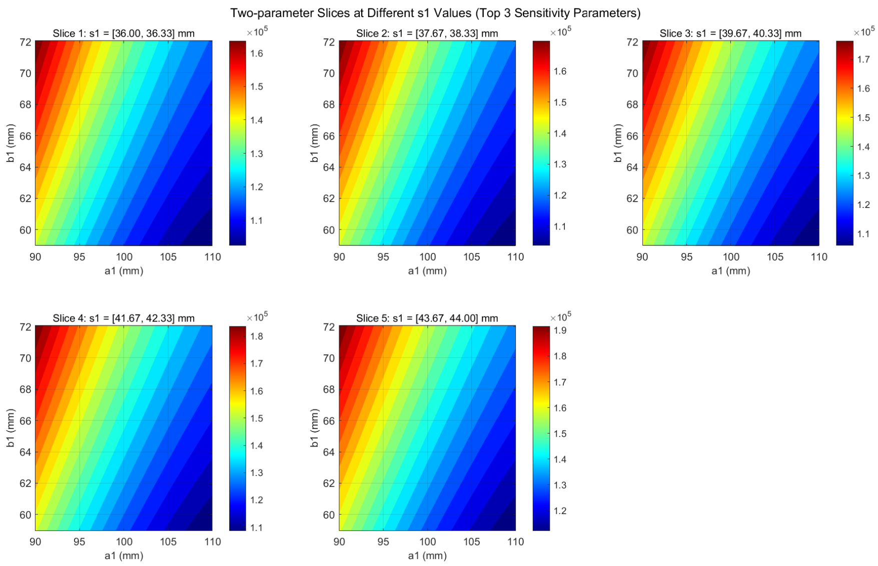

Figure 15. Combined two effect slice diagram.

5. Discussion

5.1. Proxy model validation and critical parameter sensitivity analysis

The constructed sparse PCE proxy model demonstrates a coefficient of determination increment below 0.0001 with a sample size of N = 1,500. The 10-fold cross-validation shows an average R^2 value of 0.972 and stable RMSE distribution. The proxy model's prediction accuracy exhibits a coefficient of determination R^2 of 0.978 with consistent numerical distribution. These results confirm the model's computational convergence and practical engineering applicability, providing a reliable foundation for subsequent sensitivity analysis and optimization processes.

For global sensitivity analysis, the dominant factor influencing the maximum contact force is a_1, with a main effect contribution index of 67% and a 95% confidence interval not crossing zero. b_1 and S_1 exhibit secondary influence on the maximum contact force, showing main effect contribution rates of 17% and 10%, respectively. The remaining five parameters demonstrate negligible impact rates compared to the first three, with effects approaching zero, thus being omitted from analysis. Given that the total effect aligns closely with the main effect, limited parameter interaction effects are inferred.

Regarding the single-parameter influence trends, the maximum contact force shows a significant decline with increasing a_1, exhibiting a strong negative correlation. When the size increases from 90 mm to 110 mm, the maximum contact force decreases by approximately 30%. Conversely, the maximum contact force demonstrates a significant positive correlation with increasing b_1, with the maximum contact force rising by about 20% when the size increases from 60 mm to 70 mm. The sensitivity of S_1 also shows a positive correlation with size, with marginal effects slightly intensifying in the high-value range.

To reduce impact force, minimize wear, and extend service life, priority should be given to increasing a_1 while maintaining b_1 and S_1 within specified ranges, with strict control over a_1's manufacturing tolerance to minimize maximum contact force. For multi-parameter collaborative control of maximum contact force, a strategy involving increased a_1 to regulate b_1 and restricted S_1 within defined parameters should be adopted. This approach enables regulation of the maximum contact force within the range of 1.02×10^5–1.96×10^5 N, providing clear parameter directions and quantitative references for subsequent optimization processes.

5.2. Optimization results

Based on single-parameter analysis of maximum contact force effects, a multi-parameter optimization model incorporating engineering constraints was established. The optimization model for minimizing contact force was constructed with eight design variables under finite engineering size constraints. Three weight configuration schemes—conservative, standard, and aggressive—were adopted, with the weighted multi-objective function defined as:

$$J(x) = \omega_F \cdot \widehat{F}_{max}(x) + \omega_c P_c(x) + \omega_{move} \cdot P_{move}(x). \tag{20}$$

The 8-dimensional vector $x = [\mathrm{a_1, b_1, S_1, a_2, b_2, S_2, k, \mu}]^{\mathrm{T}}$. $\widehat{F}_{max}(x)$ represents the maximum contact force response value. $P_c(x)$ as the penalty term for violating engineering constraints. $P_{move}(x)$ is the parameter modification penalty term. The weight coefficients are indicated by ω_F, ω_c, and ω_{move}. The optimization results are presented in **Table 7**. Under this scheme, the maximum contact force decreased from 138,534.85 N to 96,508.095 N, achieving a suppression effect of 29.73%.

Table 7. Optimization results table.

Parameter	Optimization results
a_1	110.0 mm
b_1	58.9 mm
S_1	36.0 mm
a_2	70.4 mm
b_2	57.8 mm
S_2	83.6 mm
k	617.72 N/m
μ	0.594

To validate the accuracy of the optimized results, the optimized parameters were incorporated into the high-fidelity model for verification calculations. As shown in **Table 8**, the computational errors between the three optimization schemes and the high-fidelity engineering model were 0.91%, 0.86%, and 0.86%, respectively, indicating that the predicted values from the forecasting model are relatively accurate.

Table 8. Comparison of predicted 1 model and engineering model calculated values.

Scheme	ω_c	ω_{move}	PCE predicts F_N	Simulation F_N	Error rate
Conservative	90	1.2	101,044.60	101,976.20	0.91%
Baseline	50	0.6	96,508.095	97,348.330	0.86%
Aggressive	25	0.2	96,508.095	97,348.330	0.86%

6. Conclusion and prospects

This study establishes a multi-parameter dynamic model, conducts dynamic simulations using acquired chamber pressure data as input conditions, and validates model accuracy through high-speed photography experiments. Based on this model, a PCE model is introduced to construct a high-precision surrogate model. Combined with Sobol global sensitivity analysis methodology, the impact of eight parameters on the maximum contact force is quantitatively evaluated. Results indicate that the elliptical major axis of the recoil groove is the primary influencing parameter affecting maximum contact force, contributing 67.2%, followed by the elliptical minor axis and linear segment of the recoil curve groove, with contribution rates of 17.1% and 10.3%, respectively. The influence rates of the remaining five parameters are negligible. An optimization model was developed based on sensitivity analysis results, reducing the maximum contact force from 138,534.85 N to 96,508.095 N with a suppression effect of 29.73%. Comparative analysis between predicted values and engineering model calculations demonstrates that error rates for all three optimization schemes remain below 1%, confirming the reliability of the optimization results.

Future research can focus on three key areas: model assumptions, model boundaries, and uncertainty sources, and engineering constraints in optimization schemes. Building upon existing models, we can integrate online learning mechanisms to achieve adaptive search for enhanced optimization efficiency. Additionally, incorporating model boundary conditions such as tolerances, material properties, and temperature parameters will establish a more comprehensive agent model framework, thereby improving model generalizability. These three dimensions warrant continued exploration.

Author contributions: All authors contributed to the study conception and design. Material preparation, data collection, and analysis were performed by JS, SY, MH, ZD and ZW. The first draft of the manuscript was written by JS. All authors commented on previous versions of the manuscript. All authors read and approved the final manuscript.

Funding: This study was supported by the National Natural Science Foundation of China (NSFC) (Grant No.: 52572450) and the Shanghai Natural Science Foundation (NSFC) (Grant No.: 23ZR1462700).

Institutional review board statement: Not applicable.

Informed consent statement: Not applicable.

Data availability statement: The data that support the findings of this study are available from the corresponding author upon reasonable request.

Conflict of interest: The authors have no relevant financial or non-financial interests to disclose.

AI use statement: During the preparation of this manuscript, the authors used DeepSeek solely for language refinement. No AI tools were used for data analysis, interpretation, or generation of scientific content. All outputs were critically reviewed and edited by the authors. The authors take full responsibility for the integrity and accuracy of the work.

References

1. Zeng J, Yang G, Wang X. Dynamics simulation and analysis for a gun with consideration of contact between roller and raceway groove. In: Proceedings of the International Conference on Mechanical Engineering and Mechanics 2007; 5–7 November 2007; Wuxi, China. pp. 1–8. (in Chinese)
2. Gong Q, Chang Z, Dan B. Kinematics simulation and analysis of the roller-gear indexing cam mechanism based on Pro/e. Journal of Hubei Automotive Industries Institute. 2008; 22(1): 41–44. (in Chinese)
3. Liu YS, He W. The Study on Dynamic Simulation of the Roller Gear Indexing Cam. Advanced Materials Research. 2012; 503–504: 44–47. doi: 10.4028/www.scientific.net/AMR.503-504.44
4. Foti P, Razavi N, Fatemi A, et al. Multiaxial fatigue of additively manufactured metallic components: A review of the failure mechanisms and fatigue life prediction methodologies. Progress in Materials Science. 2023; 137: 101126. doi: 10.1016/j.pmatsci.2023.101126
5. Wang H, Wu D, Wang F, et al. A method for determining the horizontal impact load based on the rotational speed of the aircraft's wheel in a landing gear drop test. International Journal of Crashworthiness. 2018; 23(6): 627–634. doi: 10.1080/13588265.2017.1368121

6. Chang X, Pan H, Xu J, et al. Study of Fault Identification of Clearance in Cam Mechanism. Applied Sciences. 2022; 12(15): 7420. doi: 10.3390/app12157420
7. Fedorko G, Molnár V, Blaho P, et al. Failure analysis of cyclic damage to a railway rail—A case study. Engineering Failure Analysis. 2020; 116: 104732. doi: 10.1016/j.engfailanal.2020.104732
8. Hu G, Jia C, Fang Y, et al. An experiment study on deterioration of dynamic rotational accuracy of motorized spindle. Journal of Physics: Conference Series. 2021; 1948(1): 012131. doi: 10.1088/1742-6596/1948/1/012131
9. Wu B, Zheng J, Luo TF, et al. Damage and fracture of gun barrel under wear-fatigue interaction. Journal of Physics: Conference Series. 2020; 1507(10): 102034. doi: 10.1088/1742-6596/1507/10/102034
10. Mukhtar A, Nasir H, Rashid B, et al. Development of zirconium and potassium perchlorate igniter for AP/HTPB composite propellant base bleed grain. Journal of Thermal Analysis and Calorimetry. 2019; 138(6): 3939–3947. doi: 10.1007/s10973-019-08317-2
11. Fintová S, Kuběna I, Chlupová A, et al. Very high frequency induced fatigue damage. Theoretical and Applied Fracture Mechanics. 2024; 133: 104590. doi: 10.1016/j.tafmec.2024.104590
12. Li H, Zhao Y, Jiang J, et al. Effect of frequency on the fatigue performance of bolted joints under axial excitation. Tribology International. 2022; 176: 107933. doi: 10.1016/j.triboint.2022.107933
13. Zhang P, Mi Z, Zhu Z. Stress test and fatigue analysis on flexible parts in cannon suspension device. Journal of Nanjing University of Science and Technology. 2006; 30(4): 420–423. (in Chinese)
14. Yeh JN. Simulation and application of automatic weapon transmission mechanism concept design. Journal of the Chinese Society of Mechanical Engineers. 2024; 45(1):11–21. (in Chinese)
15. Vo BV, Macko M, Dao HM. Experimental Study of Automatic Weapon Vibrations when Burst Firing. Problems of Mechatronics Armament Aviation Safety Engineering. 2021; 12(4): 9–28. doi: 10.5604/01.3001.0015.5984
16. Vu TD, Prochazka S, Krist Z, et al. Influence of Gas Port on Forces and Their Impulses Acting in an Automatic Weapon. In: Proceedings of the 2021 International Conference on Military Technologies (ICMT); 8 June 2021; Brno, Czech Republic. pp. 1–8. doi: 10.1109/ICMT52455.2021.9502832
17. Sui CJ, Cui B, Li JM, et al. Dynamics Simulation of Automatic Weapon Mechanisms and Their Impact on Shooting Accuracy. In: Proceedings of the 34th International Symposium on Ballistics; 19 May 2025; Jacksonville, FL, USA. doi: 10.12783/ballistics25/37152
18. Li B, Zhang X. Modeling and optimization of projectile in-bore motion based on a coupled method of interior ballistic multiphase flow and launch dynamics. Physics of Fluids. 2025; 37(3): 033327. doi: 10.1063/5.0257296
19. Balla J, Vitek R, Van DN, et al. Study of relationship between motion of mechanisms in gas operated weapon and its shock absorber. Defence Technology. 2024; 33: 42–54. doi: 10.1016/j.dt.2023.12.012
20. Schulze M, Dietz S, Burgermeister B, et al. Integration of Nonlinear Models of Flexible Body Deformation in Multibody System Dynamics. Journal of Computational and Nonlinear Dynamics. 2014; 9(1): 011012. doi: 10.1115/1.4025279
21. Stavropoulos P, Gerontas C, Bikas H, et al. Multi-Body dynamic simulation of a machining robot driven by CAM. Procedia CIRP. 2022; 107: 764–769. doi: 10.1016/j.procir.2022.05.059
22. Zaal JJM, Van Driel WD, Kessels FJHG, et al. Correlating Drop Impact Simulations With Drop Impact Testing Using High-Speed Camera Measurements. Journal of Electronic Packaging. 2009; 131(1): 011007. doi: 10.1115/1.3068311
23. Jayalakshmi V, Lakshmi K, Rao ARM. Dynamic force reconstruction techniques from incomplete measurements. Journal of Vibration and Control. 2018; 24(22): 5321–5344. doi: 10.1177/1077546317752709
24. Nguyen P, Vo B, Dao D, et al. Studying the dynamic characteristics of gas-operated guns using Solidworks Motion software. Vojnotehnicki glasnik. 2024; 72(3): 1066–1092. doi: 10.5937/vojtehg72-50987
25. Peherstorfer B, Willcox K, Gunzburger M. Survey of Multifidelity Methods in Uncertainty Propagation, Inference, and Optimization. SIAM Review. 2018; 60(3): 550–591. doi: 10.1137/16M1082469
26. Neves Costa J, Ambrósio J, Andrade AR, et al. Safety assessment using computer experiments and surrogate modeling: Railway vehicle safety and track quality indices. Reliability Engineering & System Safety. 2023; 229: 108856. doi: 10.1016/j.ress.2022.108856
27. Marelli S, Sudret B. UQLab: A Framework for Uncertainty Quantification in Matlab. In: Vulnerability, Uncertainty, and Risk. American Society of Civil Engineers; 2014. pp. 2554–2563. doi: 10.1061/9780784413609.257
28. Iyengar N, Rajaram D, Mavris D. Empirical Assessment of Non-Intrusive Polynomial Chaos Expansions for High-Dimensional Stochastic CFD Problems. Aerospace. 2023; 10(12): 1017. doi: 10.3390/aerospace10121017
29. Singh A, Wolf M, Jacobs G, et al. Machine learning based surrogate modelling for the prediction of maximum contact temperature in EHL line contacts. Tribology International. 2023; 179: 108166. doi: 10.1016/j.triboint.2022.108166

30. Sudret B. Global sensitivity analysis using polynomial chaos expansions. Reliability Engineering & System Safety. 2008; 93(7): 964–979. doi: 10.1016/j.ress.2007.04.002
31. Alexanderian A, Gremaud PA, Smith RC. Variance-based sensitivity analysis for time-dependent processes. Reliability Engineering & System Safety. 2020; 196: 106722. doi: 10.1016/j.ress.2019.106722
32. Bhusal R, Subbarao K. Uncertainty Quantification Using Generalized Polynomial Chaos Expansion for Nonlinear Dynamical Systems With Mixed State and Parameter Uncertainties. Journal of Computational and Nonlinear Dynamics. 2019; 14(2): 021011. doi: 10.1115/1.4041473
33. Wei Z, Chen J, Jin G, et al. Research on Dynamic Analysis and Simulation of Cam Mechanism Considering Contact Collision. Iranian Journal of Science and Technology, Transactions of Mechanical Engineering. 2024; 48(3): 1177–1190. doi: 10.1007/s40997-023-00703-4
34. Corral E, Gismeros Moreno R, Meneses J, et al. Spatial Algorithms for Geometric Contact Detection in Multibody System Dynamics. Mathematics. 2021; 9(12): 1359. doi: 10.3390/math9121359
35. Zhao R, Xie X, Yu W. Repair equipment allocation problem for a support-and-repair ship on a deep sea: A hybrid multi-criteria decision making and optimization approach. Expert Systems with Applications. 2020; 160: 113658. doi: 10.1016/j.eswa.2020.113658
36. Islam A, Belhaouari SB, Rehman AU, et al. KNNOR: An oversampling technique for imbalanced datasets. Applied Soft Computing. 2022; 115: 108288. doi: 10.1016/j.asoc.2021.108288